Additive Manufacturing 74 (2023) 103720

Contents lists available at ScienceDirect

Additive Manufacturing

journal homepage: www.elsevier.com/locate/addma

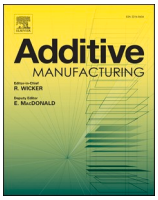

Liquid crystal display technique (LCD) for high resolution 3D printing of triply periodic minimal surface lattices bioceramics

Iman Roohani [a,*], Ali Entezari [b], Hala Zreiqat [a,*]

[a] Tissue Engineering and Biomaterials Research Unit, School of Biomedical Engineering, Faculty of Engineering, University of Sydney, Sydney, Australia
[b] School of Biomedical Engineering, Faculty of Engineering and Information Technology, University of Technology Sydney, NSW 2007, Australia

ARTICLE INFO

Keywords:
Bioceramic
3D printing
TPMS lattices
Stereolithography, vat-photopolymerization
Scaffold

ABSTRACT

The ability to fabricate highly porous bioceramic scaffolds with triply periodic minimal surface (TPMS) lattices that mimic the architecture of trabecular bone remains a challenge in ceramic additive manufacturing. The present paper describes a vat-photopolymerization technique using a high-resolution liquid crystal display (LCD), as a dynamic mask-generator, to manufacture TPMS constructs with porosities above 90%, pore sizes below 200 μm, and a minimum wall thickness of 38 μm. We systematically investigate the effects and mechanisms of processing variables, including refractive index and particle size distribution of powders on the cure depth of photosensitive slurries and dimensional accuracy prints made from hydroxyapatite and Baghdadite ($Ca_6Zr_2(SiO_7)_2O_4$) bioceramics. Our results demonstrate that the difference between the refractive index of solid particles and the photosensitive resin is a critical factor in dictating print quality and dimensional accuracy. Additionally, we showed that irrespective of the bioceramic composition, reducing the particle size from 9.0 μm (d_{50}) to 0.5 μm (d_{50}), enhances the quality of the surface finish, while decreasing the smallest feature size that can be achieved. Overall, this study presents the LCD technique as a robust and effective alternative to conventional stereolithography techniques (*i.e*, digital light processing and scanning stereolithography) for 3D fabrication of bioceramic scaffolds. It also emphasies the importance of LCD as a manufacturing technique for the implementation of advanced topological optimizations of bone scaffolds and production of patient-specific implants.

1. Introduction

The complex and multi-dimensional nature of bone defect repair presents a significant challenge in modern medicine, with deficits originating from a multitude of causes such as trauma, tumor removal, infection, or congenital anomalies. The limitations of the gold-standard treatment of autologous grafting, including limited supply, size discrepancy, and an increased risk of infection, have necessitated the emergence of synthetic grafts and solutions as preferred alternatives [1]. Bioceramics offer outstanding regenerative capabilities for bone tissue engineering, yet remarkably few have translated to the clinic, particularly for the repair of critical-size defects [1,2]. A significant obstacle to this translation is that porous bioceramics are yet to achieved the combination of natural bone's strength, toughness, and biological function [2]. The bioactivity and mechanical properties of porous bioceramics are significantly influenced by their architecture, including features such as porosity, pore size, pore geometry and interconnectivity, and strut shape and curvature [3–5]. Recently, triply periodic minimal surfaces (TPMS) structures have emerged as a promising candidate for the design of scaffolds to be used in bone regeneration, due to their mathematically defined curvature and similarity to the trabecular bone structure [6–9]. In contrast to traditional lattice structures (cubic lattices made up of struts with flat or cylindrical surfaces), TPMS structures provide lattice structures with surface characteristics similar to bone trabeculae with varying Gaussian curvatures and zero mean curvature on every surface point [6]. Changing the parameters of mathematical equations, allows for the TPMS structures to be fabricated with high interconnectivity and precisely tailored mechanical properties, porosity, pore wall thickness, and pore size [6,7,10]. As a result, TPMS-based scaffolds have the potential to provide an excellent platform for designing tissue-engineered bone scaffolds. Additionally, the large surface area of these scaffolds, allows for substantially higher release rate of bioactive ions compared to traditional strut-based structures [11]. The potential of TPMS scaffolds in biomedicine, particularly as bone substitutes and orthopedic implants, has seen a surge of interest, largely owing to their unique architectural structure which promotes

* Corresponding authors.
E-mail addresses: i.roohani@sydney.edu.au (I. Roohani), Hala.Zreiqat@sydney.edu.au (H. Zreiqat).

https://doi.org/10.1016/j.addma.2023.103720
Received 9 May 2023; Received in revised form 10 July 2023; Accepted 31 July 2023
Available online 1 August 2023

both osteogenesis and angiogenesis *in vitro* and *in vivo* [7,11–17]. In a pivotal study, Yang et al. [7] examined the potential of hyperboloidal topology in TPMS scaffolds on the osteogenic differentiation of human mesenchymal stem cells (hMSCs). The results suggest that the reorganization of the hMSC cytoskeleton, triggered by this specific geometry can instigate various cell behaviors, including enhanced osteogenesis and angiogenesis. This insight was further substantiated in a rabbit femoral defect model, revealing more pronounced new bone formation in areas with high Gaussian curvature [7], compared to that seen in regions with low Gaussian curvature in each scaffold, This insight provides additional evidence that hyperboloid topology can modulate cell morphology and nuclei biomechanics, consequently influencing cell fate. Similarly, Li et al. showcased the efficacy of β-TCP scaffolds with a gyroid architecture in boosting osteogenic differentiation of bone marrow mesenchymal stem cells (BMSCs) and the angiogenic capacity of endothelial progenitor cells. This acceleration of bone ingrowth into the scaffold pores upon implantation in the rat femur condyle was clearly demonstrated after eight weeks [14]. Building on these insights, Shen et al. showed substantial increase in the rate of magnesium ion release from Mg-doped wollastonite scaffolds with TPMS pore geometries compared to strut-designed scaffolds. They found that Diamond and Gyroid scaffolds enhanced osteogenic differentiation of BMSCs and revealed significant neo-bone tissue formation in the central pore regions within initial stages, leading to the eventual filling of the entire porous network with bone tissue compared to other type of scaffolds [11]. Further delving into the effects of pore geometries on osteogenesis and angiogenesis, Li et al. [12] fabricated wollastonite-based scaffolds with three distinct pore geometries (Gyroid, cylindrical and cubic). Of these, they discovered that gyroid scaffolds could initiate a series of cellular responses fostering angiogenesis and the development of new bone tissue in a rabbit femoral-defect model, in comparison to other geometries [12]. Broadening the scope of TPMS structures, Zhang et al. [13] demonstrated the bone-forming capabilities of Split-P TPMS structures made from hydroxyapatite. In comparison to cubic designs, the Split-P scaffolds showed better osteoconductivity and considerably higher new bone production, accompanied by significant bone metabolism activity and active bone remodeling at later stages of regeneration [13]. Collectively, these studies demonstrate the potential of optimizing TPMS designs in the creation of bioceramic scaffolds for the acceleration of osteogenesis. By exploiting the unique properties of these structures, particularly the curvature-driven responses, and combining them with advancements in 3D printing technology to achieve fine geometric features and higher porosities, we may further enhance their application potential in regenerative medicine and bone defect repair.

Additive manufacturing of bioceramics, commonly known as 3D printing, emerged to address the limitation of conventional techniques, to enable the fabrication of bioceramics scaffolds with intricate internal geometries. Current available techniques for 3D printing of bioceramics are (1) powder-bed (e.g, selective laser sintering) [18–21], (2) extrusion-based approaches (e.g, robocasting) [21,22], and (3) vat-photopolymerization (e.g, stereolithography) [23]. Using powder-bed and extrusion-based approaches, presents limitations whereby dimensional resolution, quality of surface finish, and freedom of design of complex geometries are severely restricted by instrumental factors and material properties. For example, in robocasting, the dimensional resolution is limited by the nozzle diameter [22], while in selective laser sintering, bioceramics are required to be stable at high temperatures resulting in prints typically with rough surfaces due to insufficient sintering densities [18–20].

Vat-photopolymerization, is the most potent 3D printing technology for producing bioceramic constructs with high dimensional accuracy and resolution. Over the past three years, few reports emerged on using vat-photopolymerization techniques to produce porous bioceramics with TPMS structures. However, the porosity and wall-thickness of the produced structures falls in the range of 40–60%, and ~250–2400 μm, respectively [6,7,11,24–28]. To improve the functionality of TPMS structures for bioceramics, the porosity of the constructs is best matched that of trabecular bone (70–90%), with the wall thickness substantially decreased to match that of trabecular bone struts [29]. Decreasing the wall thickness will increase the ratio of surface to volume, providing a more accurate curvature profile of the printed surfaces, as the scale of curvature of the surface in TPMS structures is inversely proportional to the square size of their unit cell. In other words, as the TPMS unit cell size (wall-thickness) decreases, the curvature of the surface becomes more pronounced. However, to accurately replicate the complexity and intricacy of TPMS structures, an additional degree of precision in the fabrication is required which is yet to be achieved. This can be achieved using two types of vat-photopolymerization techniques for manufacturing of porous bioceramics: laser scanning stereolithography (SSLA) and mask image projection stereolithography (MIP-SLA) [30–32]. The SSLA method, uses a galvanometer-controlled laser to cure a stable suspension of UV-sensitive resin and ceramic powder. This is by far the most prevalent and oldest vat-photopolymerization technique for printing bioceramics. In contrast, MIP-SLA technique cures each layer in a single exposure by projecting an image of the component's 2D cross-section onto the surface. This process significantly reduces the production time compared to SSLA, as it cures a complete layer of resin in a single step of irradiation [33]. The two main variants of MIP-SLA are digital light processing (DLP) and liquid crystal display (LCD) techniques, the former, is widely used by researchers for the 3D printing of bioceramic scaffolds [34–43]. DLP includes a digital micromirror device, acting as a dynamic mask, by selectively enabling or disabling single mirrors in an array of several million mirrors and a projector that directs the laser towards the bottom of the tank to cure the mixture of resin and ceramic particles. Most ceramic printers are based on DLP with a resolution of 2560 × 1600 pixels (pixel size of 40 × 40 μm^2) and a minimum achievable wall thickness of 100 μm. In contrast, LCD technique is the simplest and most affordable vat-photopolymerization technique which uses only a liquid crystal display, to irradiate the resin layer with UV and display itself acts as the mask generator. Every pixel in the screen is a small cell that contains molecules in a liquid-crystal state. To form a mask, each pixel can be set either to its transparent (emitting), or opaque non emitting state, by changing the orientation of the molecules. The resin in LCD is in direct contact with the display which further facilitates the printed pixels to be matched to the shape of the beam profile (Fig. 1). Moreover, there is only one mobile mechanical part in the LCD; the motorized z-positioning stage, therefore omitting the need to focus the laser beam as accurately as possible on the surface of the resin. Despite LCD clear advantage, it is yet to be adopted for printing bioceramics, as the challenge remains in the lower pixel density of existing LCDs, compared to that of the digital micromirror device used in DLP.

In this study, we utilize an LCD screen with a resolution of 7500 × 3240 pixels (1152 pixels per inch) that enabled, for the first time, the printing of complex TPMS structures with a minimum feature size of 38 μm and a porosity of up to 92%. We comprehensively studied the influence of refractive index, particle size and distribution of ceramic particles on the quality of prints. Specifically, we employed two bioceramics: hydroxyapatite and Baghdadite. Our choice of these materials was twofold. Firstly, both materials possess distinct refractive indices, offering a unique opportunity to explore how the refractive index of different ceramic compositions impacts the curing depth and the minimum feature size achievable. Secondly, hydroxyapatite and Baghdadite have been widely recognized in the literature for their exceptional biocompatibility and bioactivity, both *in vitro* and *in vivo* [44,45]. We demonstrate that the dimensional accuracy of the prints is primarily dependent on the difference between the refractive index of solid particles and the photosensitive resin, where bioceramics particle size distribution dictates the surface finish and smallest feature size achievable. To the best of our knowledge, this study is the first to employ LCD technique to accurately create TPMS geometries using bioceramic materials.

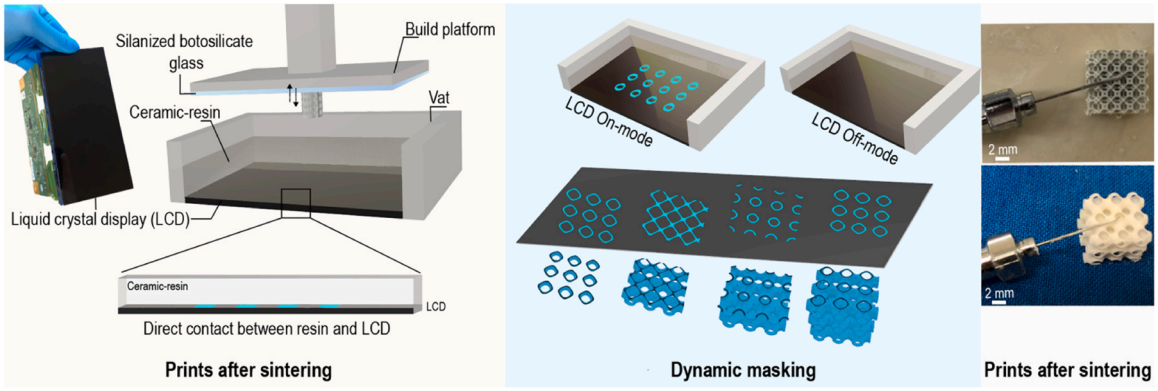

Fig. 1. Schematic diagram of the LCD printing of bioceramics featuring a simple build including one mobile part (build platform) and the high-resolution display, under the vat, that generates direct masking and selectively irradiates the surface of the ceramic resin layer by layer.

2. Materials and methods

2.1. Synthesis and processing of bioceramic powders

We prepared two types of bioceramics powders with different refra ctive indices: (1) hydroxyapatite (HA, with three distinct particle size distributions) and (2) Baghdadite (Table 1). HA particles were synthesized using a wet-precipitation method by reacting Ca- and P-bearing solutions under controlled conditions. Briefly, to prepare the Ca-bearing solution, calcium nitrate tetrahydrate ($Ca(NO_3)_2 0.4\ H_2O$, Sigma–Aldrich, > 99%) was dissolved in MQ-water (0.5 M) at 60° C for 1 h. The P-bearing solution was prepared by dissolving ammonium phosphate dibasic ($(NH_4)_2HPO_4$, Sigma–Aldrich reagent grade, ≥ 98%) in MQ-water (0.3 M) at 60° C for 4 h. After the solutions reached 60° C, P-solution was added dropwise to the P-solution under continuous stirring and pH was kept at 7.45 ± 0.25 by the addition of 1 M ammonia solution. The reaction medium was kept at 60° C for 1 h and then precipitates were filtered and collected in a filter paper and washed several three times with MQ-water.

The formed cake was dried at 120 °C for three days and then calcined at 1000 °C for 1 h. Baghdadite particles were fabricated using a sol-gel technique. Chemicals including tetraethyl orthosilicate (TEOS, $(C_2H_5O)_4Si$), zirconia oxide nitrate ($ZrO(NO_3)_2$), calcium nitrate tetrahydrate were purchased from Sigma-Aldrich. TEOS was hydrolysed by the addition of 2 M nitric acid and ethanol in a molar ratio of 1: 8: 0.16, respectively. Then the $ZrO(NO_3)_2$ and $Ca(NO_3)_2{\cdot}4\ H_2O$ were added into the beaker containing hydrolysed TEOS at a molar ratio of 1:3:2, respectively. The solution was stirred for 5 h at room temperature and then sealed and placed in an eclectic at 60 °C for 1 day for sol-gel transformation. The obtained gels dried at 100 °C for 2 days and then calcined at 1150 °C for 3 h. To obtain three distinct particle size distributions for HA powders (HA9, HA2, and HA0.5), calcined particles were refined by a high-energy planetary ball mill (Retsch PM400, Germany). For HA9, 200 g of calcined powder, 250 mL of ethanol and 8 zirconia balls with a diameter of 15 mm were added to zirconia-coated stainless-steel jars. After milling for 3 h at 150 rpm, the slurry was passed through a − 63 μm stainless sieve and dried at 120 °C for 2 days. For HA2, 150 g of calcined powder, 250 mL of ethanol and 12 zirconia balls with a diameter of 15 mm were added to jars. After milling for 3 h at 250 rpm, the balls were replaced with 200 g of 3 mm zirconia balls and milling continued for an additional 2 h. After milling, the slurry passed through a − 20 μm stainless sieve and dried at 120 °C for 2 days. For HA0.5, 100 g of calcined powder, 250 mL of ethanol and 12 zirconia balls with a diameter of 15 mm were added to jars. After milling for 3 h at 250 rpm, balls were replaced with 200 g mixture of 1 mm, 0.5 mm and 0.1 mm zirconia balls and milling continued for an additional 3 h. After milling, the slurry passed through a − 20 μm stainless sieve and dried at 120 °C for 2 days. The same methodology as for HA9 was applied to BGH.

2.2. Scaffold design and fabrication

2.2.1. Silanization of the building platform

Borosilicate glass slides (Ted Pella, INC) were used to enhance the adhesion of prints to the building platform. Glass slides with a thickness of 1 mm were silanized and secured on the printer building platform using double-sided tape. For silanization, glass slides were washed with ethanol three times and cleaned in an ultrasonic cleaner in a methanol bath for 2 min. The glass slides were then transferred into a beaker containing 100 mL methanol, 5 mL acetic acid and 3 mL of 3-(Trimethoxysilyl) propyl methacrylate and incubated for 45 min (All chemicals were purchased from Sigma-Aldrich). After incubation, glass slides were removed from the beaker and washed with methanol three times followed by rinsing using ethanol. Slides were wiped gently and stored in a desiccator.

2.2.2. Ceramic-resin slurry preparation and processing

A photocurable slurry was formulated using bioceramic powder (40 vol%), sodium polyacrylate (1.5 wt% for HA9 and Baghdadite, 2 wt % for HA2, and 3 wt% for HA0.5, where the weight percentages are relative to the weight of the dried powder; Sigma-Aldrich), acrylate oligomer, 4-(1-oxo-2-propenyl)-morpholine, and Bis(1,2,2,6,6-pentamethyl-4-piperidinyl) sebacate (Phrozen Technology, Taiwan). This resulted in a slurry exhibiting viscosity ranging from 1200 mPa.s (for HA9) to 1800 mPa.s (for HA0.5), with shear thinning behavior observed at low shear rates (1–10 S^{-1}). To create a slurry using HA9 powder, the powder was gradually introduced to the liquid phase while

Table 1
Designation and physical properties of bioceramic powders used for LCD printing.

Designation	Ceramic	Density (g/cm^3)	10th percentile particle size d_{10} (μm)	50th percentile particle size d_{50} (μm)	90th percentile particle size d_{90} (μm)	Refractive index, n
BGH	Baghdadite	3.48	4.4	8.4	13.2	1.67
HA9	Hydroxyapatite	3.18	4.8	9.0	16.4	1.63
HA2	Hydroxyapatite	3.18	0.4	2.6	4.8	1.63
HA0.5	Hydroxyapatite	3.18	0.1	0.5	1.2	1.63

being mechanically mixed to prevent the formation of lumps and agglomerates, thereby ensuring a uniform suspension. A quantity of 200 mL of this suspension and eight 15 mm diameter zirconia balls were transferred into the milling jars, which have a maximum capacity of 500 mL. The suspension was then homogenized at 110 rpm for 8 h before being passed through a − 75 μm stainless steel sieve to yield the slurry. The same procedure was used to produce a slurry from Baghdadite powder. For the HA2 and HA0.5 slurry, the powder was gradually introduced into the liquid phase within milling jars, each containing fifteen 15 mm diameter zirconia balls. This mixture was then stirred for 5 min at 110 rpm. After all the powder was incorporated, the mixture was homogenized for 8 h at 110 rpm, and then sieved through a − 53 μm stainless steel sieve to obtain the slurry.

2.2.3. 3D printing and postprocessing

The scaffolds were fabricated using a custom-set up LCD-based stereolithography system using a 7.1-inch linear projection LED display (wavelength 460 nm, Phrozen Technology, Taiwan) with the highest resolution of 22 μm (1152 PPI, 7500 × 3240 pixels). The thickness of a single layer could be selected in the range of 10–100 μm. For all prints, we chose a layer thickness of 50 μm as an optimum thickness for high-speed printing and adequate z-axis resolution. In order to systematically study the influence of printing variables (particle size, refractive index of particles, and exposure time) on cure depth and quality of prints, we designed a mask (STL file is available in SI) using Autodesk Fusion 360 containing arrays of square and sphere pores from 1000 μm to 20 μm in size. To ascertain the curing depth, we first loaded the STL file of the circular film benchmark (provided in the supplementary information) onto the printer. Subsequently, we added the ceramic slurry into the vat. After each designated exposure time, the film was carefully removed, thoroughly cleaned with isopropyl alcohol (IPA), and subjected to sonication to ensure complete removal of any uncured slurry. The thickness of the film, which corresponds to the curing depth, was then measured using an outside micrometre. To ensure accuracy, we confirmed these measurements using a microscope. This process was repeated for four samples per exposure time to provide a reliable average curing depth. The LCD intensity was not adjustable, therefore for analysis of cure depth and dimensional accuracy, we printed the constructs at different UV exposure time which was manually set using slicing software. We designed sheet-based lattices of TPMS structures, inlcuding the three common types: Gyroid, Schwarz, and Diamond. The porosities of these structures ranged from 65% to 92%, with variations achieved by altering the unit cell thickness (from 100 μm to 400 μm) in nTopology software. We constructed strut-based lattices with Fluorite, Kelvin, and Octet structures with an average strut size of 250 μm. These unit cells are commonly used for design of porous bone scaffolds and metallic implants and as the representative of sheet-based and strut-based lattice designs. The LCD printing parameters were optimized to ensure high-quality prints. The exposure time was set to 6 s, with a layer height of 50 μm. We introduced two initial bottom layers with an extended exposure time of 100 s to enhance the adhesion of the construct to the build platform. The bottom lift distance was set to 6 mm, and the build platform's lifting speed was set to 60 mm/min. These parameters were meticulously chosen to balance print speed, construct integrity, and fine feature resolution.

LCD printing was conducted to produce the designs and to obtain scaffolds with final dimensions close to the nominal ones after sintering, shrinkage compensation factors equal to 1.1 and 1.3 along the x-y and z-axis were applied. For constructs with strut size and wall thickness greater than 300 μm, the glass substrate was detached from the building platform, immersed upside down in a tank filled with ethanol. The tank was then agitated for 2 min. Following this, compressed air was used to eliminate any remaining uncured resin within the microcavities. This cycle was repeated until all pores were verified to be open, ensuring thorough cleaning of the construct without compromising the integrity of the thin walls or struts. For constructs with feature sizes less than 300 μm, a more delicate approach was utilized to preserve the structural integrity of constructs. The glass substrate was again submerged in an ethanol tank, this time without agitation, for a duration of 2 min. Compressed air, at a substantially lower pressure, was then gently employed to remove the excess uncured resin. This procedure was likewise repeated until all scaffolds were entirely clean. Next, constructs were carefully removed from the glass slides using an ultrasound cutter to preserve the intricate structures and to avoid physical damage and the formation of cracks in struts and walls. The samples went through a multiple-stage heat treatment schedule (Fig. 2) to burn the organic components and consolidate the scaffolds using an elevator high-temperature electric furnace (LABEC, Australia).

2.3. Characterizations

The scaffolds were chemically characterized by X-ray diffraction (XRD) technique using a Philips X'PERT MPD diffractometer (Cu Kα radiation: λ = 0.154056 nm at 40 kV and 30 mA) over the 2θ range of 20–50° at a scan rate of 0.02°/min. The scaffold structure and struts were analysed using scanning electron microscopy (SEM, Zeiss Sigma HD FEI). To analyze the internal structure of scaffolds using SEM, we used a diamond saw to cut the scaffolds. The μCT-based models were created based on the μ-CT images of the 3D-printed scaffold specimens. Each scaffold was scanned using a SkyScan 1172 (Kontich, Belgium) at an 8 μm voxel size resolution with 100 kV, 100 μA, and a 1.0 mm aluminium filter. Projection images were integrated for 885 ms every 0.5° over a full 180° rotation. Each raw data set was then reconstructed into an axial stack saved as greyscale BMP images using SkyScan's reconstruction software NRecon (Kontich, Belgium) for further processing. Reconstruction parameters were kept constant for each scan of a specimen to provide consistent greyscale factors for the analysis. Each set of reconstructed images was then imported into the image-processing software ScanIP (Simpleware Ltd, Exeter, UK). The porosity and surface area of each scaffold was characterized in the image processing software ScanIP (Simpleware Ltd, Exeter, UK). In ScanIP, the statistical tools of Volume Fraction and Surface Area were used to determine the porosity and surface area of scaffolds, respectively. It should be noted that the same threshold range was used for the segmentation of different scaffolds to provide a consistent measurement of porosity for all scaffolds. The wall thickness of each scaffold was characterized and displayed in the image processing software ScanIP (Simpleware Ltd, Exeter, UK). In ScanIP, the Wall Thickness analysis tool for masks or surface objects was utilized. For this purpose, a raycasting algorithm was implemented by firing a ray normal to the surface of the model towards the material side. The point where this ray hits the other surface is considered the hit point. The distance between the start and the hit point is the "ray

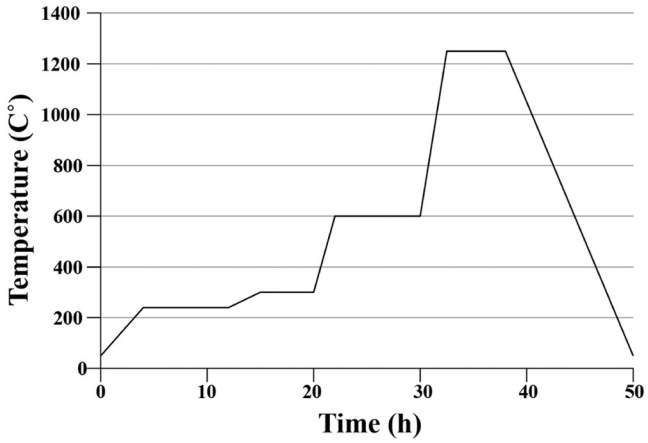

Fig. 2. Heat treatment schedule used for burning off the cured ceramic resin and sintering HA scaffolds.

thickness".

3. Results and discussion

The stability of the slurry, consisting of a mixture of ceramic powder and UV-curable resin, is a key factor in achieving successful vat-photopolymerization of bioceramics. Typically, ceramic particles tend to aggregate and separate from the resin over time, which can compromise the stability of the slurry. This is especially important when printing large objects as the slurry will remain in the vat for a longer period, thereby increasing the risk of particle separation and sedimentation during the vat polymerization process. Particle separation can result in a lower quality print as they (1) create regions of the printed part that have a higher concentration of ceramic particles and regions that have a lower concentration, (2) lead to the clustering of ceramic particles and in turn the formation of defects such as cracks or voids, in the printed part and (3) generate a rougher surface finish on the printed part. In this study, we verified the particle size distribution and the presence of dispersant on the stability of the slurries. We demonstrated that slurry made from HA9 without using dispersant, became unstable after 1 h, leading to the formation of two distinct phases: an opaque phase, primarily composed of ceramic powder, and a transparent phase, predominantly resin (as seen in Fig. 3a). In contrast, reducing the particle size (HA0.5), delayed this separation to 48 h, without using the dispersant. After the addition of dispersant, slurries made from HA9 and HA0.5, were stable for up to two weeks with no visible separation between the ceramic particles and the resin, and with similar curing behaviour to the freshly prepared slurries (Fig. 3b). Segregation in layers of ceramic powder and resin is directly related to the settling velocity (v_g) of the particles; a measure of how quickly the particles in the slurry settle under the influence of gravity. This can be explained by Eq. (1) derived from combined Richardson-Zaki (R–Z) equation and Stokes' law:

$$v_g = \frac{1}{18} \quad \frac{(\rho_c - p_m) g d^2}{\eta} \quad (1-\varphi)^n \tag{1}$$

Where φ, ρ_c and ρ_m are solid particle volume fraction, density of particle and resin, respectively. d is the diameter of particle, η is the resin viscosity and n is Richardson and Zaki index. As indicated by Eq. (1), the settling rate of particles in resin is inversely proportional to the viscosity of the resin and the size of the particles, with a more significant reduction in settling rate for smaller particles which is proportional to the square of the particle diameter.

The curing behaviour of the slurry is another important parameter in the vat-photopolymerization of ceramics. The dimensional accuracy and soundness of the print are directly be related to the curing depth, determined mainly by the formulation of the slurry. Slurries formulated in this study contain a large volume of solid particles (40 vol%), necessary to reduce the shrinkage of the printed parts during the sintering process. An inadequate concentration of solid particles in the resin can result in excessive shrinkage during sintering, causing warping or cracking of the printed parts. However, solid particles actively contribute to scattering the incident light and prevent its efficient absorption by the photoinitiator which leads to a reduction of cure depth.

Generally, particle size distribution, shape, refractive index and volume percentage of ceramic particles influence the nature of inter-

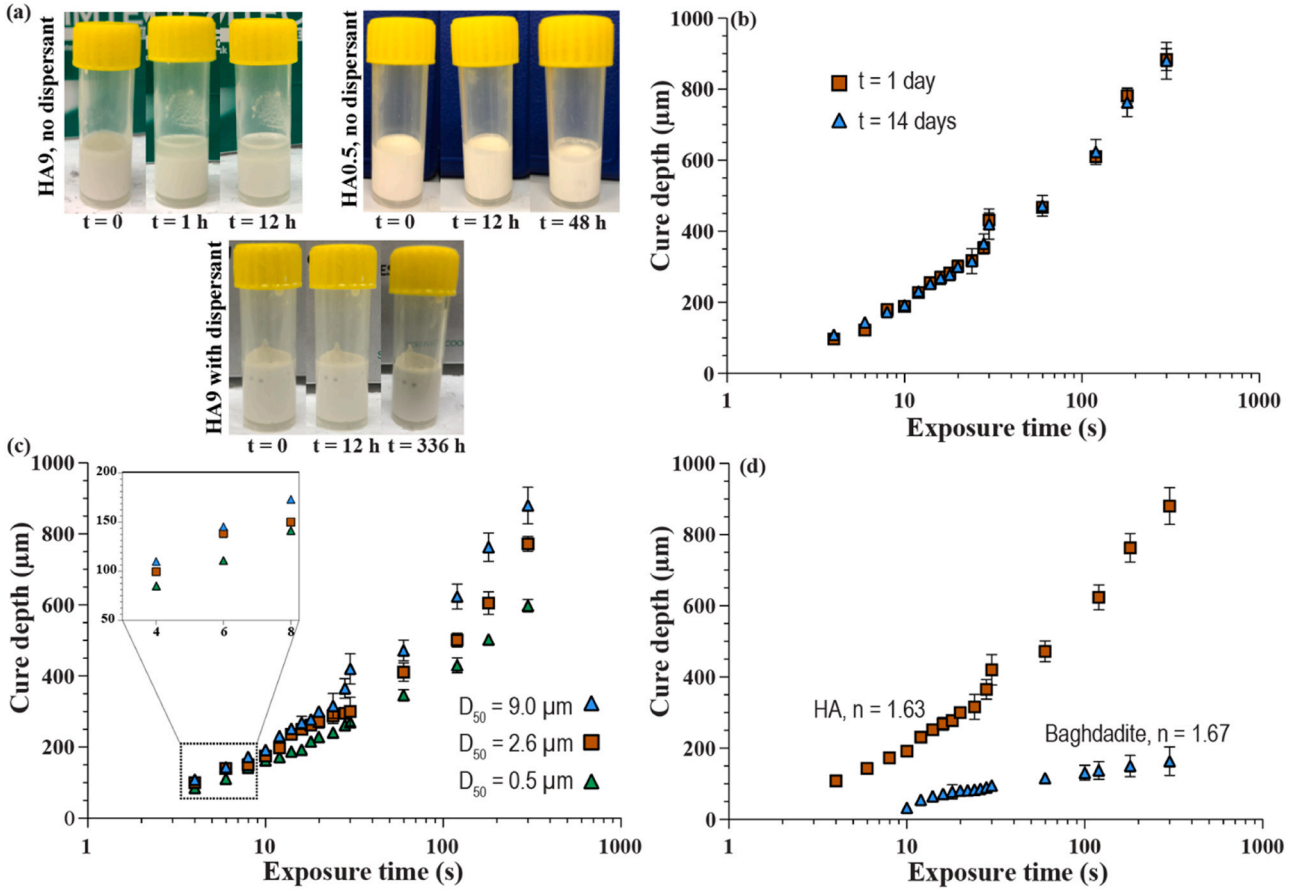

Fig. 3. (a) Slurry stability of HA9 (left panel, no dispersant), HA9 (right panel, with dispersant), and HA9 (bottom panel, with dispersant). The apparent color variation is due to lighting differences and does not reflect an actual change in the slurry color. (b) The cure depth of a slurry made from HA9 compared with the cure depth of the same slurry kept on the bench for 14 days. (c) The cure depth of slurries prepared by HA9, HA2.6 and HA0.5 after UV irradiation. (d) the cure depth of slurries made from HA in comparison to Baghdadite at a range of exposure times to UV irradiation.

action with incident light and hence the cure depth. We measured the cure depth of slurries consisting of HA particles with three sizes (D_{50} = 9.0 μm, 2.6 μm, and 0.5 μm) at different exposure times to UV (Fig. 3c) and observed that cure depth decreased with decreasing the particle size. However, this difference was not as striking, compared to the change in the cure depth of slurries caused by a mismatch in the refractive index of the ceramic constituents (Fig. 3d). We assessed the cure depth of two slurries made from two bioceramics; HA (n = 1.63) and Baghdadite (n = 1.67), both with close particle size distributions. The cure depth of the slurries made from HA was ~5–10 times higher over the range of exposure time tested, compared to that of Baghdadite. The incident light is also *absorbed* by the ceramic particles, further lowering the cure depth (C_d). Since the typical thickness of the resin layer in single photon vat-photopolymerization of ceramics is between 10 and 100 μm, the C_d of the ceramic resin must be higher than this to facilitate printing. The Griffith and Halloran [46], modelled the depth of cure for a concentrated suspension of ceramic particles in a photocurable resin:

$$C_d = \frac{2}{3}\ \frac{d_{50}}{Q\varphi}\ \ \frac{n_0^2}{\Delta n^2}\ln\left(\frac{E_0}{E_{crit}}\right) \quad (2)$$

Where d_{50} is the average particle size, Δn^2 is the square of the refractive index difference between the ceramic and UV sensitive resin, φ the volume fraction of solid, E_0 the energy density, Q is the scattering efficiency term and E_{crit} is the minimum energy density required for setting the resin. n_0 is the refractive index of the resin. According to Eq. (2), it is established that the cure depth decreases as the particle size decreases and the difference between the refractive index of ceramics and resin increases. However, this relationship is inversely proportional to Δn^2, where a minor difference in the refractive indexes of ceramics and resin can result in a significant impact on the cure depth, potentially surpassing the effects caused by variations in particle size and inter-particle spacing.

A benchmark mask was created to examine the printing accuracy of high-resolution LCD, particularly in producing curved and straight edges with various sizes (Fig. 4a and b). The mask contains two arrays of square and circular pores, each having a length and diameter ranging from 1000 μm to 20 μm (nominal x-y resolution of the LCD). HA9, HA2 and HA0.5 models were printed using LCD technique from HA and Baghdadite powders. We divided square and circular pores into two zones: large pores, zone 1 (1000 μm, 900 μm, 800 μm and 700 μm) and small pores, zone 2 (600 μm, 500 μm, 400 μm, and 300 μm). For all bioceramics compositions and particle sizes, the geometry and size of pores in zone 1 were comparable to the designed mask except for ones printed by DLP (Fig. 4c); an expected finding due to lower resolution of DLP compared to LCD printer. We demonstrated that the surface finish quality was significantly improved by reducing the particle size. HA0.5 prints surface finish was smooth, in contrast to scattered protrusions and

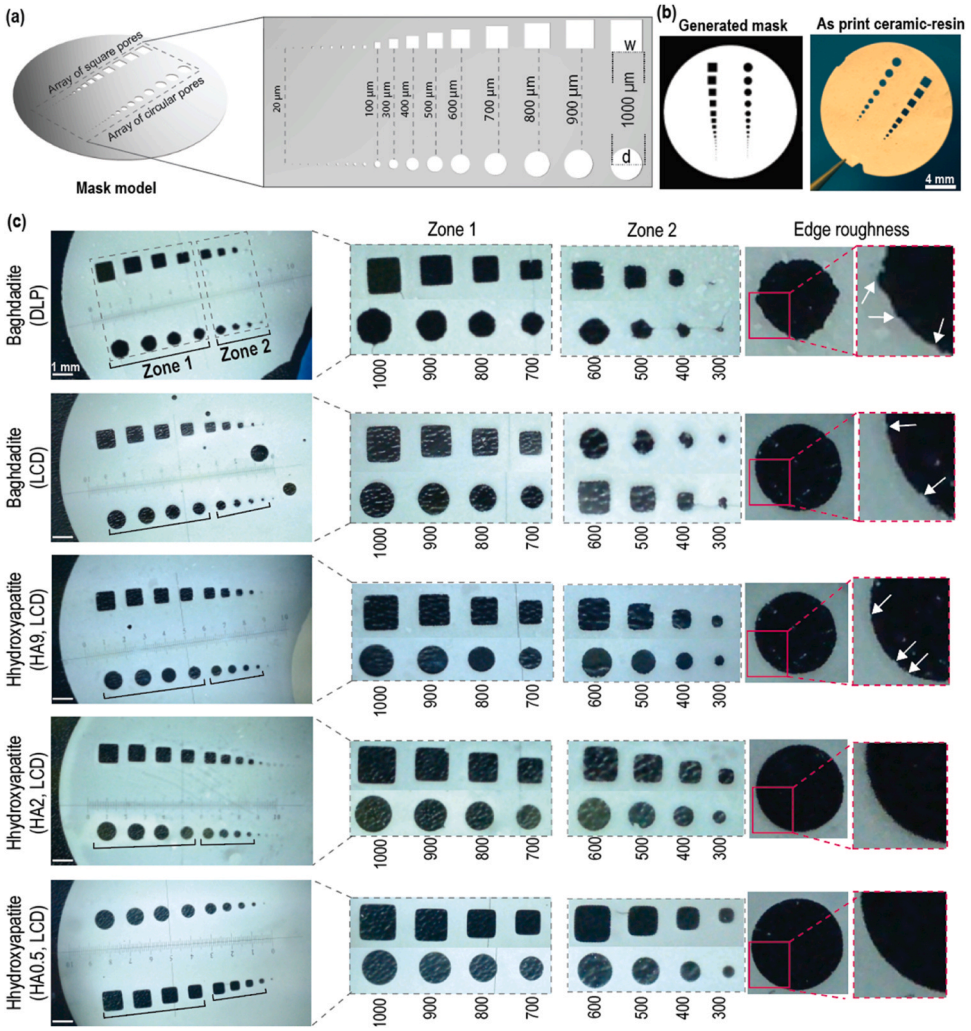

Fig. 4. (a) The designed mask containing arrays of circular and square pores in varying sizes (STL file is provided in SI). (b) Generated mask by the slicing software (left) and image of the printed sample by LCD technique(right). (c) Representative images of prints using slurries made from Baghdadite and HA powders with different particle sizes using DLP and LCD techniques (left panel) and representations of the quality of printed features and surface finish of samples (right panel).

dips on the surface of pores made by HA2, HA9 and Baghdadite. Analyzing the square and circular arrays printed with LCD technique using Baghdadite and HA9 slurries, and featuring similar particle size distribution, we noticed discernible differences. Specifically, when utilizing Baghdadite, which possesses a higher refractive index, the accuracy started to diminish in features smaller than 500 μm. The pores of 300 μm in diameter were filled, blurring the distinguishing boundaries between squares and circles. Conversely, for the HA9 prints, the 300-micron pores and squares remained clearly distinguishable. This contrast demonstrates the considerable influence of the refractive index difference between the selected ceramic powder and resin on the achievement of precise small feature sizes.

Next, we quantified the accuracy of the printing based on the dimensional deviation between the model and prints (pore diameter for circular pores and pore length for square pores) (Fig. 5). We analysed more than 2000 pore and square arrays and demonstrated that reducing the particle size led to a higher dimensional accuracy, albeit with reduced ability to print the minimum feature size achievable. The slurries made from small particle sizes, scattered the incident light effectively at the higher exposure times (overexposed condition) leading to faster deterioration in accuracy. In contrast, better accuracy was achieved when slurries with large and medium particle sizes were used under high UV exposure times regardless of powder composition. The difference in refractive index between the resin and the ceramic powder influenced mostly the ability to achieve minimum feature size. The minimum achievable pore size with more than 90% shape accuracy for HA2 and HA9 slurries was 100 μm, this contrasts with 400 μm for slurry made from the Baghdadite. We successfully printed HA9 with pore size down to 50 μm, however, longer exposure time diminished the ability to print fine pore sizes.

Bone regeneration is highly dependent on the internal design and surface properties of 3D-printed scaffolds. The structure of vertebral trabecular bone, for instance, resembles cubic grid-like structures, with vertical struts bearing loads in compression and horizontal ones providing reinforcement [47]. However, CAD-based cubic grid-like models are limited, as their sharp junctions create unnaturally high stress concentrations and real human bone remodels itself to minimize these junctions. As such, a skeletal graph of another member of the minimal surface family, the 'primitive' surface, is proposed as a better model for generating structures that resemble vertebral trabecular bone. TPMS structures possess a zero mean curvature and can be repeated periodically in three perpendicular directions. Furthermore,

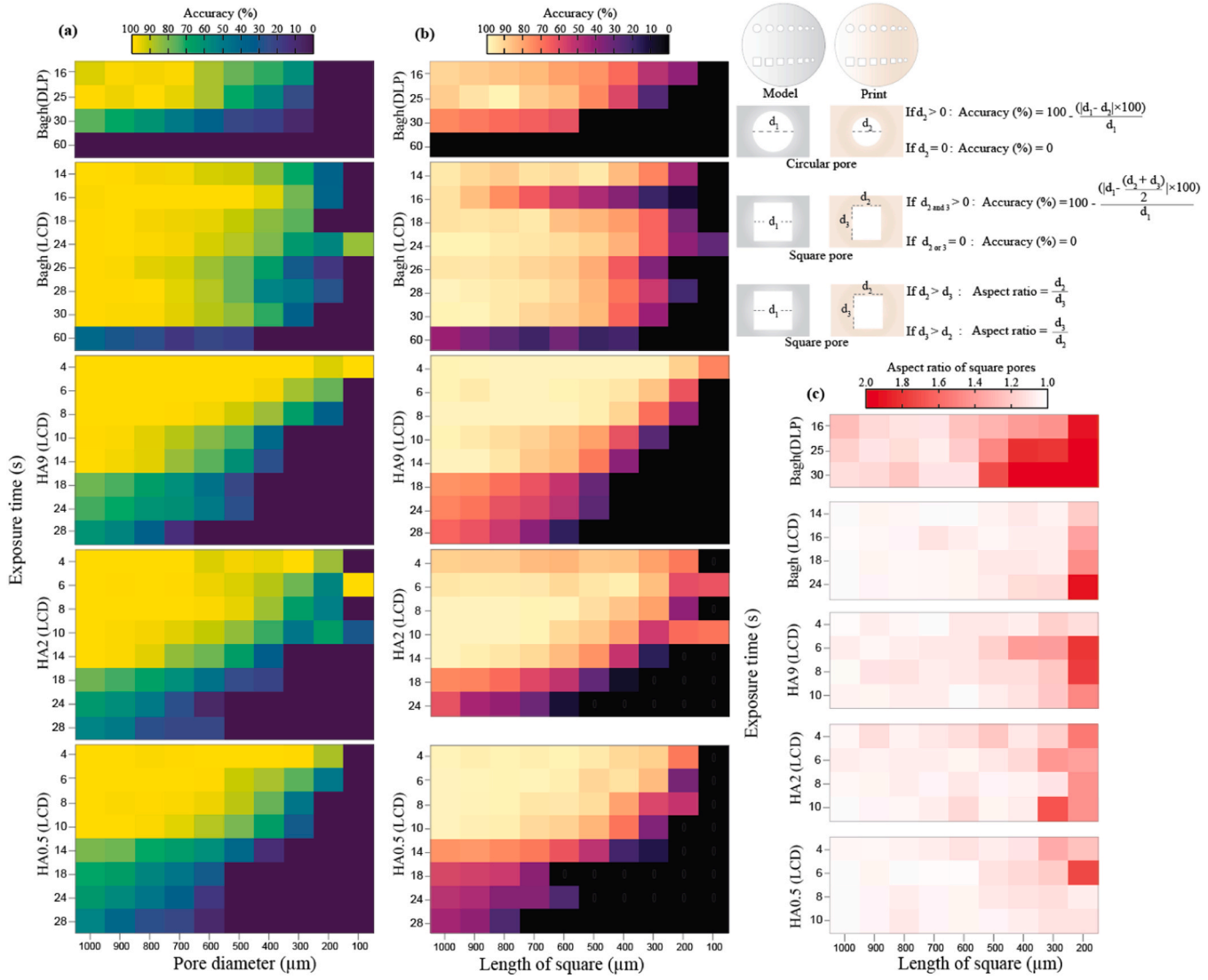

Fig. 5. Colour map of the shape accuracy of prints compared to 3D models calculated based on the difference in diameter and length of (a) circular and (b)square pores as well as (c) aspect ratio of square pores for slurries made from HA and Baghdadite powders using LCD and DLP techniques and for different UV exposure times.

TPMS-based scaffolds offer precise control over pore architecture and scaffold morphology, allowing for computer-controlled solidification of layer-by-layer ceramic-resin upon light irradiation. These advances in 3D printing technology offer promising avenues for the creation of scaffolds that closely resemble the internal structure of human bone, ultimately leading to better bone regeneration outcomes. Using a slurry made from HA0.5, we fabricated two types of porous constructs: (1) sheet-based lattices (TPMS structures: Gyroid, Schwarz and Diamond) and (2) strut-based lattices (Fluorite, Kelvin, and Octet) (Fig. 6). Scanning electron microscopy (SEM) revealed that high-resolution LCD printing closely reproduce sheet- and strut-based lattice structures containing fine feature and pore sizes.

To evaluate the accuracy of 3D printed TPMS structures, we performed high resolution micro-CT scanning of the sintered specimens. Fig. 7 depicts the reconstructed micro-CT models visualizing the detailed 3D structures of the TPMS structures 3D printed using the LCD technique. To quantify the wall thickness throughout each structure, a raycasting algorithm was implemented using the image processing software ScanIP (Simpleware Ltd, Exeter, UK). Fig. 7 illustrates the contour of wall thickness for each sintered sample, revealing unprecedented structural details that have not been attainable by other stereolithography techniques for bioceramics. The Schwarz unit cells had a uniform wall thickness with an average size of ~120 μm and total porosity of 88%. The average minimum diamond wall thickness reached ~70 μm and the total porosity of 90%, while the average wall thickness size for Gyroid constructs was ~60 μm achieving a substantially high porosity of 92% (Figure S1) [6]. To further quantify the wall thickness inside the 3D printed TPMS structures, a 2D micro-CT image located approximately in the middle of each TMPS structure is depicted in the right panel of Fig. 7, representing a random cross-section within each structure. The minimum wall thickness in these random cross-sections is 160 μm, 104 μm, and 85 μm for Schwarz, diamond, and Gyroid structures, respectively.

The surface-to-volume (S/V) ratio is an alternative physical

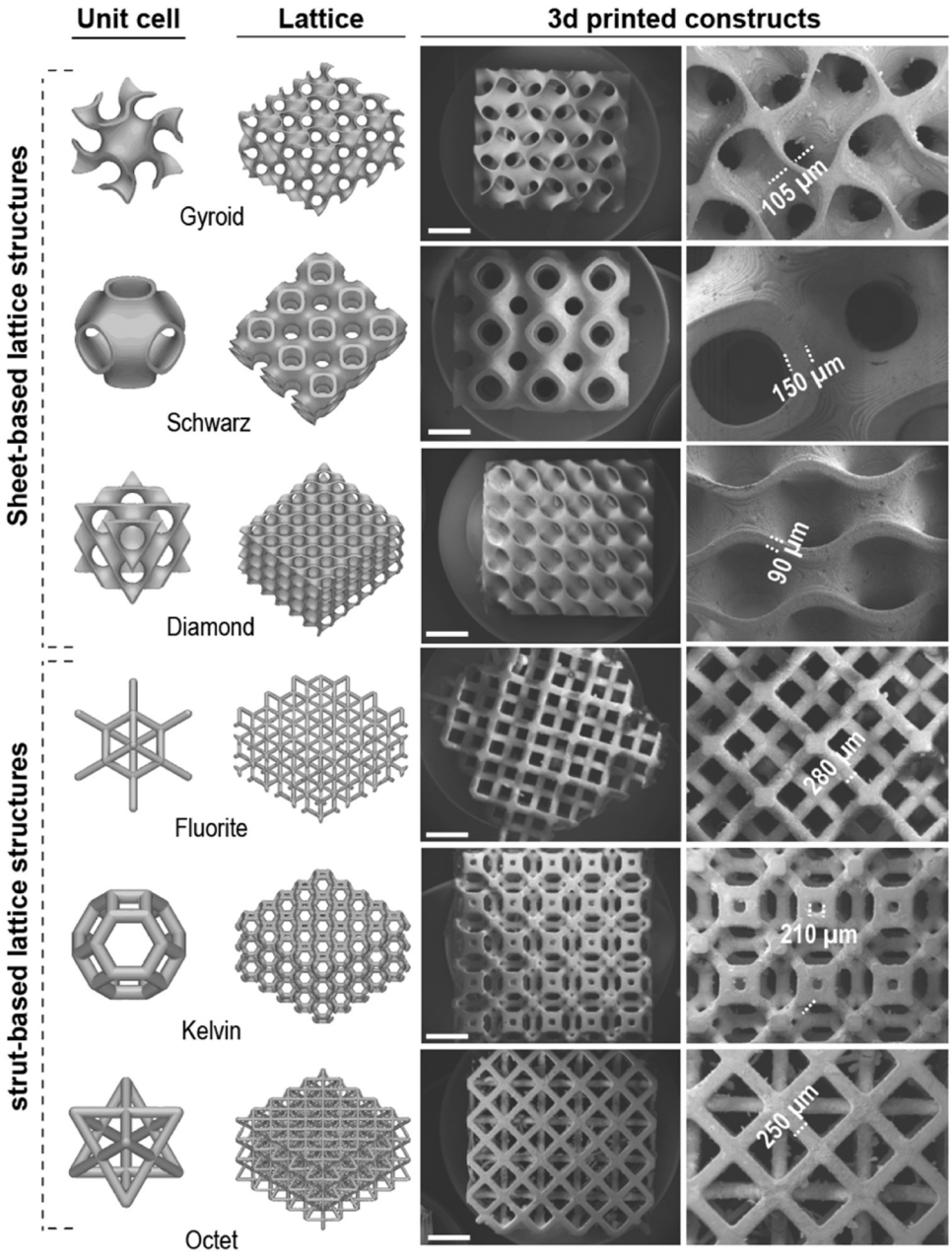

Fig. 6. SEM micrographs displaying the structure of 3D models and sintered scaffolds, scale bar = 1 mm.

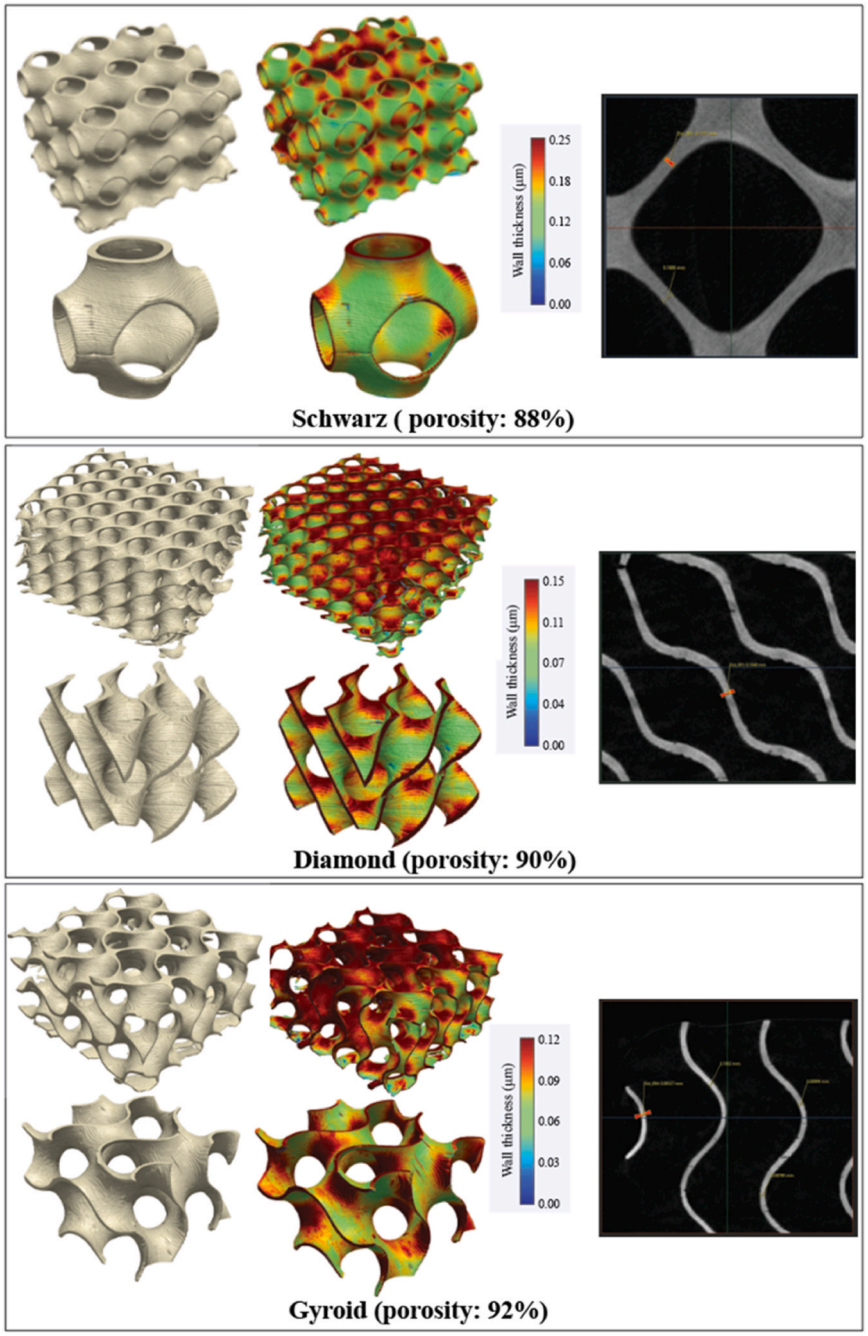

Fig. 7. Micron-CT images of highly porous sintered TPMS bioceramic constructs printed by the LCD technique.

parameter for a bone scaffold that can aid in the selection of an optimal candidate for bone tissue scaffolds among various lattice structures. This is because a higher S/V ratio corresponds to a greater surface area for accommodating the cells, adhesion of growth factors and cytokines and ingrowth of tissue. The S/V ratio of bone ranges from 1 to 6 mm^{-1} in bones, whereas in vertebrae, it varies from 2 to 3 mm^{-1} [48]. The maximum S/V ratios achieved for Schwarz, Diamond, and Gyroid were 2.3, 2.8 and 4.1 which is well-within the S/V range of bone. To further examine the minimum wall thickness of the structures, we performed SEM on the fabricated TPMS samples. Fig. 8 depicts an SEM image of the fracture surface related to a sintered gyroid structure representing a wall thickness as fine as 38 μm close to the nominal resolution of the LCD.

The minimal wall thickness that can be achieved depends on the specific geometry and design of the struts or walls within the porous structure. Generally, strut-based designs, wherein the strut size (thickness) is uniform across the Z direction, pose some limitations in terms of the minimum size that can be achieved stably. This minimum size is typically substantially greater than the nominal resolution of the printer (LCD is 22 μm). This limitation primarily arises due to insufficient support beneath the struts, which precludes the possibility of achieving a strut size equivalent to a single line scan. In contrast, sheet-based designs permit variations in wall thickness in the Z direction. This flexibility allows for adequate support for the layers beneath, enabling us to achieve smaller wall thicknesses. However, it should be noted that when the designated thickness approaches the nominal voxel resolution, the structure tends to become exceedingly fragile and unstable. Although scaffolds with TPMS structures show potential for bone tissue regeneration, fabrication of these structures effectively through vat-photopolymerization techniques namely SLA and DLP poses difficulties. The creation of thin walls and small channel sizes that are

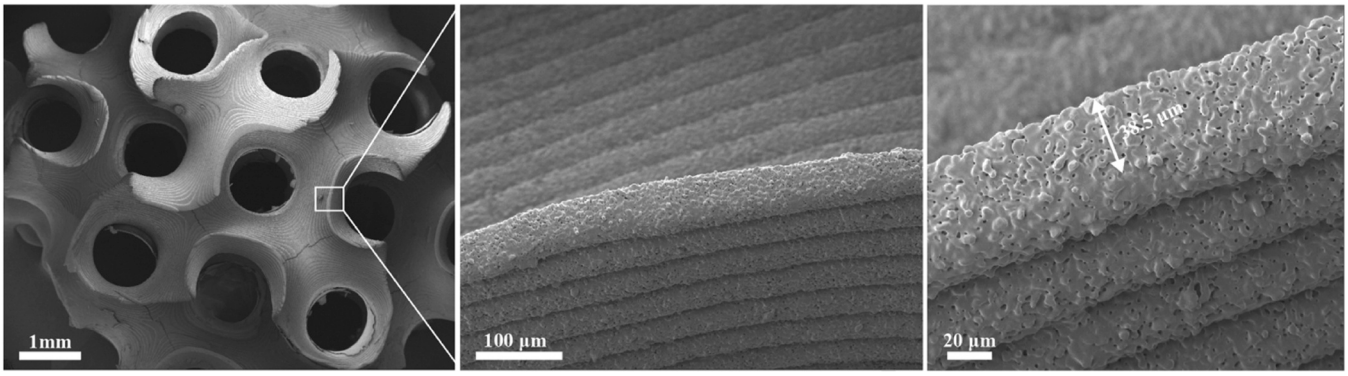

Fig. 8. SEM micrographs of the fracture surfaces of a sintered HA Gyroid scaffold at different magnifications. The presence of cracks observed in these images is an outcome of the sectioning process using a diamond saw.

necessary for vascularization stretches the limits of commercially available printers. Additionally, challenges arise from printing the designs on an inverted architecture, removing residual slurry from the tiny pores, and ensuring the components are free of impurities and have predictable dimensions after firing. In this study, various processing windows were evaluated to address these challenges using high resolution LCD technique. Overall, the LCD technique addressed the current limitation in designing bioceramics due to limitations in creating structures with feature sizes smaller than 100 µm [49]. This study demonstrates that LCD technique enables a high degree of control over the internal architecture, shape, and geometry of bioceramic scaffolds, making it possible to finely tune the mechanical and biological properties of bioceramic implants.

4. Conclusion

In conclusion, our research presents a significant advancement in the field of vat-photopolymerization techniques, where we leverage a high-resolution liquid crystal display (LCD) to manufacture TPMS constructs with remarkable precision and intricacy. Our process ensures the fabrication of scaffolds with porosities exceeding 90%, pore sizes below 200 µm, and a minimum wall thickness of 38 µm, lending unprecedented structural details previously unattainable by other stereolithography techniques for bioceramics. Notably, the introduction of this advanced technique enables the generation of precisely curved features that are integral to the design of TPMS structures, effectively overcoming the resolution limitations inherent to existing ceramic printing technologies. It thereby allows for an improved replication of theoretical design curvatures, which in turn, drives superior exploitation of curvature-dependent biological and mechanical functionality. Our detailed evaluation of 3D printed TPMS structures using high-resolution micro-CT scanning further reinforces these findings. The reconstructed models offer invaluable insights into the intricate 3D structures achievable using the LCD technique. The potential and flexibility of this method is demonstrated in generation of TPMS constructs such as the Schwarz unit cells with an average wall thickness of ~120 µm and total porosity of 88%, Diamond structures with a minimum wall thickness of ~70 µm and total porosity of 90%, and Gyroid structures exhibiting a wall thickness of ~60 µm and a high porosity of 92%. Additionally, the surface-to-volume (S/V) ratios achieved for the various structures fall within the physiological range for bone, suggesting that these TPMS scaffolds could serve as optimal candidates for bone tissue engineering applications. In particular, the Gyroid structure demonstrated a maximum S/V ratio of 4.1, implying a significantly large surface area for accommodating cells, adhesion of growth factors and cytokines, and tissue ingrowth. In summary, this study opens new possibilities in the functional design and manufacturing of advanced bioceramic scaffolds with optimal topologies that could significantly contribute to the development of patient-specific implants and bone tissue engineering strategies. Our work also underscores the potential benefits and challenges associated with this novel technique, thereby enhancing the knowledge body in this field. We believe that our findings lay the groundwork for future research aimed at advancing the potential of TPMS structures in bioengineering applications.

CRediT authorship contribution statement

Roohani Iman: Investigation, Funding acquisition, Formal analysis, Data curation, Conceptualization.

Declaration of Competing Interest

The authors declare that they have no known competing financial interests or personal relationships that could have appeared to influence the work reported in this paper.

Data Availability

Data will be made available on request.

Acknowledgements

The authors acknowledge the Australia Research Council (DP220102876), University of Sydney Nano Institute/Kickstarter. The authors acknowledge the technical and scientific assistance of Sydney Microscopy & Microanalysis, the University of Sydney node of Microscopy Australia.

Appendix A. Supporting information

Supplementary data associated with this article can be found in the online version at doi:10.1016/j.addma.2023.103720.

References

[1] I. Roohani, G.C. Yeo, S.M. Mithieux, A.S. Weiss, Emerging concepts in bone repair and the premise of soft materials, Curr. Opin. Biotechnol. 74 (2022) 220–229, https://doi.org/10.1016/j.copbio.2021.12.004.
[2] K. Lin, R. Sheikh, S. Romanazzo, I. Roohani, 3D printing of bioceramic scaffolds-barriers to the clinical translation: from promise to reality, and future perspectives, Mater. (Basel) 12 (2019) 2660.
[3] I. Roohani, E. Newsom, H. Zreiqat, High-resolution vat-photopolymerization of personalized bioceramic implants: new advances, regulatory hurdles, and key recommendations, Int. Mater. Rev. (2023), https://doi.org/10.1080/09506608.2023.2194744.
[4] S.J.P. Callens, R.J.C. Uyttendaele, L.E. Fratila-Apachitei, A.A. Zadpoor, Substrate curvature as a cue to guide spatiotemporal cell and tissue organization, Biomaterials 232 (2020), 119739.

[5] X. Lin, S. Romanazzo, K. Lin, C. Kelly, J.J. Gooding, I. Roohani, Elliptical supracellular topographies regulate stem cells migratory pattern and osteogenic differentiation, Materialia 14 (2020), 100870.

[6] C.A. Hoel, S.K. Peterson, R. Rose, E. Telfeyan, L.A. Boyd, J.-H. Her, D.J. Erno, C. Bhushan, J.S. Martinez, B.M. Davis, et al., Processing vat polymerized triply periodic minimal surface scaffolds of hydroxyapatite, Adv. Eng. Mater. 25 (2023), https://doi.org/10.1002/adem.202200956.

[7] Y. Yang, T. Xu, H.-P. Bei, L. Zhang, C.-Y. Tang, M. Zhang, C. Xu, L. Bian, K.W.-K. Yeung, J.Y.H. Fuh, et al., Gaussian curvature-driven direction of cell fate toward osteogenesis with triply periodic minimal surface scaffolds, Proc. Natl. Acad. Sci. U. S. A. 119 (2022), https://doi.org/10.1073/pnas.2206684119.

[8] M. Vafaeefar, K.M. Moerman, M. Kavousi, T.J. Vaughan, A morphological, topological and mechanical investigation of gyroid, spinodoid and dual-lattice algorithms as structural models of trabecular bone, J. Mech. Behav. Biomed. Mater. 138 (2023), 105584, https://doi.org/10.1016/j.jmbbm.2022.105584.

[9] S.J.P. Callens, D.C. Tourolle né Betts, R. Müller, A.A. Zadpoor, The local and global geometry of trabecular bone, Acta Biomater. 130 (2021) 343–361, https://doi.org/10.1016/j.actbio.2021.06.013.

[10] J. Shi, L. Zhu, L. Li, Z. Li, J. Yang, X. Wang, A TPMS-based method for modeling porous scaffolds for bionic bone tissue engineering, Sci. Rep. 8 (2018), https://doi.org/10.1038/s41598-018-25750-9.

[11] M. Shen, Y. Li, F. Lu, Y. Gou, C. Zhong, S. He, C. Zhao, G. Yang, L. Zhang, X. Yang, et al., Bioceramic scaffolds with triply periodic minimal surface architectures guide early-stage bone regeneration, Bioact. Mater. 25 (2023) 374–386, https://doi.org/10.1016/j.bioactmat.2023.02.012.

[12] Y. Li, J. Li, S. Jiang, C. Zhong, C. Zhao, Y. Jiao, J. Shen, H. Chen, M. Ye, J. Zhou, et al., The Design of Strut/TPMS-Based Pore Geometries in Bioceramic Scaffolds Guiding Osteogenesis and Angiogenesis in Bone Regeneration, Mater. Today Bio 20 (2023), https://doi.org/10.1016/j.mtbio.2023.100667.

[13] Q. Zhang, L. Ma, X. Ji, Y. He, Y. Cui, X. Liu, C. Xuan, Z. Wang, W. Yang, M. Chai, et al., High-strength hydroxyapatite scaffolds with minimal surface macrostructures for load-bearing bone regeneration, Adv. Funct. Mater. (2022), https://doi.org/10.1002/adfm.202204182.

[14] M. Li, J. Jiang, W. Liu, X. Huang, X. Wu, W. Wei, H. Zhu, J. Zhang, J. Xiao, H. Dai, Bioadaptable Bioactive Glass-β-Tricalcium Phosphate Scaffolds with TPMS-Gyroid Structure by Stereolithography for Bone Regeneration, J. Mater. Sci. Technol. 155 (2023) 54–65, https://doi.org/10.1016/j.jmst.2023.01.025.

[15] F.S.L. Bobbert, K. Lietaert, A.A. Eftekhari, B. Pouran, S.M. Ahmadi, H. Weinans, A. A. Zadpoor, Additively Manufactured Metallic Porous Biomaterials Based on Minimal Surfaces: A Unique Combination of Topological, Mechanical, and Mass Transport Properties, Acta Biomater. 53 (2017) 572–584.

[16] C.N. Kelly, A.S. Lin, K.E. Leguineche, S. Shekhar, W.R. Walsh, R.E. Guldberg, K. Gall, Functional repair of critically sized femoral defects treated with bioinspired titanium gyroid-sheet scaffolds, J. Mech. Behav. Biomed. Mater. 116 (2021), https://doi.org/10.1016/j.jmbbm.2021.104380.

[17] K. Song, Z. Wang, J. Lan, S. Ma, Porous Structure Design and Mechanical Behavior Analysis Based on TPMS for Customized Root Analogue Implant, J. Mech. Behav. Biomed. Mater. 115 (2021), https://doi.org/10.1016/j.jmbbm.2020.104222.

[18] K. Shahzad, J. Deckers, Z. Zhang, J.-P. Kruth, J. Vleugels, Additive manufacturing of zirconia parts by indirect selective laser sintering, J. Eur. Ceram. Soc. 34 (2014) 81–89, https://doi.org/10.1016/j.jeurceramsoc.2013.07.023.

[19] R. Gmeiner, U. Deisinger, J. Schönherr, B. Lechner, R. Detsch, A.R. Boccaccini, J. Stampfl, Additive manufacturing of bioactive glasses and silicate bioceramics, J. Ceram. Sci. Technol. 6 (2015) 75–86, https://doi.org/10.4416/JCST2015-00001.

[20] S. Bose, S. Vahabzadeh, A. Bandyopadhyay, Bone tissue engineering using 3D printing, Mater. Today 16 (2013) 496–504, https://doi.org/10.1016/j.mattod.2013.11.017.

[21] A. Kumar, S. Mandal, S. Barui, R. Vasireddi, U. Gbureck, M. Gelinsky, B. Basu, Low temperature additive manufacturing of three dimensional scaffolds for bone-tissue engineering applications: processing related challenges and property assessment, Mater. Sci. Eng. R. Rep. 103 (2016) 1–39, https://doi.org/10.1016/j.mser.2016.01.001.

[22] S.-I. Roohani-Esfahani, P. Newman, H. Zreiqat, Design and Fabrication of 3D Printed Scaffolds with a Mechanical Strength Comparable to Cortical Bone to Repair Large Bone Defects, Sci. Rep. 6 (2016), https://doi.org/10.1038/srep19468.

[23] Diptanshu; Young, E.; Ma, C.; Obeidat, S.; Pang, B.; Kang, N. Ceramic Additive Manufacturing Using Vat Photopolymerization 2018, *1*.

[24] Y. Zhang, Q. Zhang, F. He, F. Zuo, X. Shi, Fabrication of cancellous-bone-mimicking β-tricalcium phosphate bioceramic scaffolds with tunable architecture and mechanical strength by stereolithography 3D printing, J. Eur. Ceram. Soc. 42 (2022) 6713–6720, https://doi.org/10.1016/j.jeurceramsoc.2022.07.033.

[25] D. Van hede, B. Liang, S. Anania, M. Barzegari, B. Verlée, G. Nolens, J. Pirson, L. Geris, F. Lambert, 3D-printed synthetic hydroxyapatite scaffold with in silico optimized macrostructure enhances bone formation in vivo, Adv. Funct. Mater. 32 (2022), https://doi.org/10.1002/adfm.202105002.

[26] Y. Li, R. Wu, L. Yu, M. Shen, X. Ding, F. Lu, M. Liu, X. Yang, Z. Gou, S. Xu, Rational design of nonstoichiometric bioceramic scaffolds via digital light processing: tuning chemical composition and pore geometry evaluation, J. Biol. Eng. 15 (2021).

[27] F. Lu, R. Wu, M. Shen, L. Xie, M. Liu, Y. Li, S. Xu, L. Wan, X. Yang, C. Gao, et al., Rational design of bioceramic scaffolds with tuning pore geometry by stereolithography: microstructure evaluation and mechanical evolution, J. Eur. Ceram. Soc. 41 (2021) 1672–1682.

[28] M. Shen, W. Qin, B. Xing, W. Zhao, S. Gao, Y. Sun, T. Jiao, Z. Zhao, Mechanical Properties of 3D Printed Ceramic Cellular Materials with Triply Periodic Minimal Surface Architectures, J. Eur. Ceram. Soc. 41 (2021) 1481–1489, https://doi.org/10.1016/j.jeurceramsoc.2020.09.062.

[29] Y. Li, Y. Xiao, C. Liu, The horizon of materiobiology: a perspective on material-guided cell behaviors and tissue engineering, Chem. Rev. 117 (2017) 4376–4421.

[30] H.-B. Sun, S. Kawata, Two-Photon Photopolymerization and 3D Lithographic Microfabrication, Adv. Polym. Sci. 170 (2004) 169–273.

[31] X. Song, Y. Chen, T.W. Lee, S. Wu, L. Cheng, Ceramic fabrication using mask-image-projection-based stereolithography integrated with tape-casting, J. Manuf. Process. 20 (2015) 456–464.

[32] G. Mitteramskogler, R. Gmeiner, R. Felzmann, S. Gruber, C. Hofstetter, J. Stampfl, J. Ebert, W. Wachter, J. Laubersheimer, Light curing strategies for lithography-based additive manufacturing of customized ceramics, Addit. Manuf. 1 (2014) 110–118, https://doi.org/10.1016/j.addma.2014.08.003.

[33] F. Zhang, Z. Li, M. Xu, S. Wang, N. Li, J. Yang, A Review of 3D Printed Porous Ceramics, J. Eur. Ceram. Soc. 42 (2022) 3351–3373, https://doi.org/10.1016/j.jeurceramsoc.2022.02.039.

[34] Y.Y. Filippov, A.M. Murashko, P.V. Evdokimov, T.V. Safronova, V.I. Putlayev, Stereolithography 3D Printed Calcium Pyrophosphate Macroporous Ceramics for Bone Grafting, Open Ceram. 8 (2021).

[35] C. Goutagny, S. Hocquet, D. Hautcoeur, M. Lasgorceix, N. Somers, A. Leriche, Development of calcium phosphate suspensions suitable for the stereolithography process, Open Ceram. 7 (2021), https://doi.org/10.1016/j.oceram.2021.100167.

[36] I.I. Preobrazhenskiy, A.A. Tikhonov, P.V. Evdokimov, A.V. Shibaev, V.I. Putlyaev, DLP printing of hydrogel/calcium phosphate composites for the treatment of bone defects, Open Ceram. 6 (2021), https://doi.org/10.1016/j.oceram.2021.100115.

[37] R. Felzmann, S. Gruber, G. Mitteramskogler, P. Tesavibul, A.R. Boccaccini, R. Liska, J. Stampfl, Lithography-based additive manufacturing of cellular ceramic structures, Adv. Eng. Mater. 14 (2012) 1052–1058, https://doi.org/10.1002/adem.201200010.

[38] P. Tesavibul, R. Felzmann, S. Gruber, R. Liska, I. Thompson, A.R. Boccaccini, J. Stampfl, Processing of 45S5 Bioglass® by Lithography-Based Additive Manufacturing, Mater. Lett. 74 (2012) 81–84, https://doi.org/10.1016/j.matlet.2012.01.019.

[39] R. Gmeiner, G. Mitteramskogler, J. Stampfl, A.R. Boccaccini, Stereolithographic ceramic manufacturing of high strength bioactive glass, Int. J. Appl. Ceram. Technol. 12 (2015) 38–45, https://doi.org/10.1111/ijac.12325.

[40] J.W. Halloran, Ceramic stereolithography: additive manufacturing for ceramics by photopolymerization, Annu. Rev. Mater. Res. 46 (2016) 19–40.

[41] P. Navarrete-Segado, M. Tourbin, C. Frances, D. Grossin, Masked stereolithography of hydroxyapatite bioceramic scaffolds: from powder tailoring to evaluation of 3D printed parts properties, Open Ceram. 9 (2022), 100235, https://doi.org/10.1016/j.oceram.2022.100235.

[42] J. Schmidt, H. Elsayed, E. Bernardo, P. Colombo, Digital light processing of wollastonite-diopside glass-ceramic complex structures, J. Eur. Ceram. Soc. 38 (2018) 4580–4584.

[43] F. Baino, G. Magnaterra, E. Fiume, A. Schiavi, L.-P. Tofan, M. Schwentenwein, E. Verné, Digital light processing stereolithography of hydroxyapatite scaffolds with bone-like architecture, permeability, and mechanical properties, J. Am. Ceram. Soc. 105 (2022) 1648–1657.

[44] S.I.I. Roohani-Esfahani, C.R.R. Dunstan, B. Davies, S. Pearce, R. Williams, H. Zreiqat, Repairing a critical-sized bone defect with highly porous modified and unmodified baghdadite scaffolds, Acta Biomater. 8 (2012) 4162–4172, https://doi.org/10.1016/j.actbio.2012.07.036.

[45] S. Bhat, U.T. Uthappa, T. Altalhi, H.-Y. Jung, M.D. Kurkuri, Functionalized porous hydroxyapatite scaffolds for tissue engineering applications: a focused review, ACS Biomater. Sci. Eng. 8 (2022) 4039–4076, https://doi.org/10.1021/acsbiomaterials.1c00438.

[46] M.L. Griffith, J.W. Halloran, Scattering of ultraviolet radiation in turbid suspensions, J. Appl. Phys. 81 (1997) 2538–2546, https://doi.org/10.1063/1.364311.

[47] G. Bini, F. Bini, R. Bedini, A. Marinozzi, F. Marinozzi, A topological look at human trabecular bone tissue, Math. Biosci. 288 (2017) 159–165, https://doi.org/10.1016/j.mbs.2017.03.009.

[48] A. Timercan, V. Sheremetyev, V. Brailovski, Mechanical properties and fluid permeability of gyroid and diamond lattice structures for intervertebral devices: functional requirements and comparative analysis, Sci. Technol. Adv. Mater. 22 (2021) 285–300, https://doi.org/10.1080/14686996.2021.1907222.

[49] A.D. Lantada, A. De Blas Romero, M. Schwentenwein, C. Jellinek, J. Homa, Lithography-Based Ceramic Manufacture (LCM) of auxetic structures: present capabilities and challenges, Smart Mater. Struct. 25 (2016), https://doi.org/10.1088/0964-1726/25/5/054015.